Journal of Power Sources 425 (2019) 130–137

Contents lists available at ScienceDirect

Journal of Power Sources

journal homepage: www.elsevier.com/locate/jpowsour

Multifunctional atomic force probes for Mn^{2+} doped perovskite solar cells

Yinghui Wu[a,b], Wei Chen[b,c], Zunyuan Wan[b], Aleksandra B. Djurišić[c], Xiyuan Feng[b], Liyu Liu[a], Guo Chen[a], Ruchuan Liu[a,*], Zhubing He[b,**]

[a] Chongqing Key Laboratory of Soft Condensed Matter Physics and Smart Materials, College of Physics, Chongqing University, No. 55, University City South Rd., Chongqing, 401331, China
[b] Department of Materials Science and Engineering, Shenzhen Key Laboratory of Full Spectral Solar Electricity Generation (FSSEG), Southern University of Science and Technology, No. 1088, Xueyuan Rd., Shenzhen, 518055, China
[c] Department of Physics, The University of Hong Kong, Pokfulam, Hong Kong, China

HIGHLIGHTS

- Scanning Kelvin Probe Microscopy is used to test the open circuit voltage of films.
- Conductive atomic force microscopy is used to study the short-circuit of films.
- Electrostatic force microscopy is used to distinguish the surface charge change of films.

ARTICLE INFO

Keywords:
Perovskite solar cells
SKPM
C-AFM
EFM

ABSTRACT

Doping in organic–inorganic perovskite semiconductors is an effective method to tailor their optoelectronic properties. In this work, manganese-doped perovskite films with different Mn/Pb ratios ranging from 0% to 2% were systematically studied. The device performance of 0.2% Mn-doped devices was improved compared to that of a device without Mn. However, a further increase of the doping concentration induced a decrease in performance. Several characteristics (especially different scanning probe microscopy characteristics) reveal that an increased dopant concentration results in reduced crystallinity and a change in the film morphology and causes a deterioration in photovoltaic performance for higher dopant concentrations. In the best-performing samples (0.2%), a shift in the valence band level and band gap are found which are responsible for the increased open circuit voltage, while increased grain boundaries and lower surface charge density are responsible for a small reduction in the short circuit current. Thus, multifunctional scanning probe microscopy approaches, combined with different film characterization techniques, offer us effective tools to investigate the impact of doping in the perovskite materials and the corresponding device performance.

1. Introduction

Doping is a powerful technique to modulate carrier concentrations in semiconductors in microelectronics, and it is extensively used in the inorganic solar cell industry. $MAPbI_3$ perovskite with the formula ABX_3 is one of the most promising materials among the emerging photovoltaics [1]. Referring to this idea, there have been several attempts at doping in perovskite materials with versatile ions to replace each site of ABX_3 [2–6]. For example, by the incorporation of trivalent cations (Bi^{3+}, Au^{3+} and In^{3+}), the band gap and conductivity of $MAPbBr_3$ single crystals can be tuned over 0.3 eV and four orders of magnitude, respectively [7]. These properties of the perovskite materials can also be varied by doping with Sb^{3+} ions [8]. Another trivalent cation Al^{3+} improved the power conversion efficiency (PCE) of $MAPbI_3$ solar cells to 19.1% by reducing the microstrain and passivating the grain boundaries [9]. The impact of monovalent cation dopants, such as Li^+, Na^+, K^+, Cu^+, Ag^+, on the performance of perovskite solar cells (PSCs) was also explored [10–14]. The influence of divalent metal ions on the performance of PSCs, especially transition metal ions with ion radii similar to lead, were also studied. It was found that Co^{2+} doping [15] and Hg^{2+} doping [16] can enhance the performance of cells. Although these reports above examined the doping effect of various elements on

* Corresponding author.
** Corresponding author.
E-mail addresses: yinghui@cqu.edu.cn (Y. Wu), chenw7@mail.sustc.edu.cn (W. Chen), wanzunyuan@163.com (Z. Wan), dalek@hku.hk (A.B. Djurišić), 11753009@mail.sustc.edu.cn (X. Feng), lyliu@cqu.edu.cn (L. Liu), wezer@cqu.edu.cn (G. Chen), phyliurc@cqu.edu.cn (R. Liu), hezb@sustc.edu.cn (Z. He).

https://doi.org/10.1016/j.jpowsour.2019.04.009
Received 8 September 2018; Received in revised form 20 March 2019; Accepted 3 April 2019
0378-7753/

PSCs via performance variation and some indirect evidence and achieved high conversion efficiency (PSCs), further information is needed to understand the impact of doping in perovskite materials on the characteristics of PSCs and the relationship between device performance, film properties and dopant introduction.

Atomic force microscopy (AFM) is a useful tool for the comprehensive study of film properties. One of the AFM scanning modes, namely scanning Kelvin probe microscopy (SKPM), has become a routine tool for the characterization and optimization of nanophase-separated organic and hybrid photovoltaic blends [17]. It also was also widely used to measure the work function distribution across the surface of a sample [18–22]. SKPM also has been successfully applied to estimate the charge transfer in the perovskite/hole/electron transporting materials (HTM/ETM) interface [23–25]. In addition, electrostatic force microscopy (EFM) can offer direct information of relative charge concentration, and imaging [26,27]. EFM has been successfully applied to quantitatively estimate carrier density in P3HT and pentacene nanostructures [28,29], CdSe@ZnS quantum dots [30], silicon nanorods [31], and so on.

In this work, divalent ions Mn^{2+} were employed as dopants in $MAPbI_3$ perovskite to modulate the film morphology and device performance. Experimental results found that a small amount of Mn^{2+} ionic doping in $MAPbI_3$ improved the device performance via enhancing the open circuit voltage and fill factor, while slightly decreasing the short circuit current density. EFM along with conductive atomic force microscopy (C-AFM) and SKPM were employed to investigate the doping effect of Mn^{2+} on the structure of $MAPbI_3$ films by modulating doping concentration via the Mn/Pb ratio of precursors in solution.

2. Experimental

2.1. Materials

CH_3NH_3I was purchased from Luminescence Technology Corp (Taipei, Taiwan). $PC_{61}BM$ (99.5%) was sourced from Derthon Optoelectronic Materials Science Technology Co LTD (Shenzhen, China). Poly(3,4-ethylenedioxythiophene)-poly(styrenesulfonate) (Clevios PVP AI 4083, PEDOT:PSS) was obtained from Heraeus Group (Hanau, Germany). Unless specially specified, other chemical agents were purchased from Sigma Aldrich (Shanghai, China) or Alfa Aesar (Shanghai, China).

2.1.1. Intrinsic and Mn doped $MAPbI_3$ films

CH_3NH_3I and PbI_2 (at a molar ratio of 1:1) at a concentration of 1 M in a mixture of DMF and DMSO (2:1 v/v) at 70 °C was used as the perovskite precursor solution and filtered by a 0.22 μm Polytetrafluoroethylene (PTFE) syringe filter. Different concentrations of $MnCl_2$ solutions were freshly prepared in DMF. This is achieved by preparing and comparing different concentrations of manganese chloride solutions. The same volume of $MnCl_2$ solution was added to the filtered precursor solution to maintain a constant precursor solution concentration in a series of doping experiments. A certain amount of PbI_2 in the solution was replaced with an equimolar amount of $MnCl_2$ to form a mixed film. All procedures described above were carried out in a nitrogen glove box.

2.2. Materials characterization

X-ray diffractometer (XRD) patterns were measured with a multifunction powder X-ray diffractometer (Rigaku Smartlab 9 KW, Tokyo, Japan). Absorption spectra were recorded by a UV/Vis/NIR spectrometer (LAMBDA 950, PerkinElmer Waltham, Massachusetts, USA) in the wavelength range of 550–800 nm. Room temperature photoluminescence (PL) and time-resolved PL spectra were recorded by fluorescence spectrophotometer (FS5, Edinburgh Instruments Livingston, UK).

A 405 nm pulsed laser was selected as excitation source for the time resolved PL measurement. A Coherent Sapphire SF 532 nm 150 CW laser was used for excitation. The surface work functions of perovskite films with different Mn concentrations were collected by ultraviolet photoelectron spectroscopy (UPS) (AXIS Ultra DLD, KRATOS Analytical Manchester, UK). The perovskite films on indium tin oxide (ITO)/Poly (3,4-ethylenedioxythiophene)/poly(styrenesulfonate) (PEDOT:PSS) substrates were characterized by a MIRA3 TESCAN (Carl ZeissAG, Jena, Germany) transmission electron microscope. The cross-section scanning electron microscopy (SEM) was performed by a commercial focused-ion beam (FEI Helios Nanolab 600i, Chicago, Illinois, USA) operating at 30 kV and subsequently imaged with the electron beam of the same instrument using an accelerating voltage of 5 kV. Electrochemical impedance spectroscopy (EIS) was measured using an electrochemical workstation (Zennium, Zahner, Jena, Germany) with an amplitude of 5 mV under dark conditions. The resulting impedance spectra were fitted using the ZView software (Scribner Associates Inc., Southern Pines, NC, USA).

2.3. Device fabrication

Patterned ITO substrates were cleaned by sonicating in deionized water, acetone and ethanol, each for 20 min, followed by blow-drying with nitrogen and oxygen plasma treatment for 15 min. PEDOT:PSS was filtered with a 0.22 μm PTFE syringe filter immediately prior to use. Then, PEDOT:PSS was spin-coated on the cleaned and dried ITO substrates at 5000 rpm for 30 s, followed by thermal annealing at 140 °C for 15 min in air. The mixed-metal perovskite solutions were spin-coated on the PEDOT:PSS at 3500 rpm for 35 s with dripping of chlorobenzene (250 μL) as the anti-solvent during the last 15 s of the spinning process, and the substrate was then annealed on a hot plate at 100 °C for 10 min. Next, a layer of $PC_{61}BM$ (20 mg/mL in chlorobenzene) was spin-coated on top, followed by annealing at 100 °C for 30 min. ZrAcac (1 mg/mL in methanol) was then drop-casted on the top of $PC_{61}BM$ films at 5000 rpm for 30 s. Finally, silver electrodes (100 nm) were thermally evaporated through a shadow mask. The device area was ~10 mm^2 as defined by the shadow mask.

2.4. Device measurements

The current–voltage (J − V) curves were recorded using a Keithley (Solon, Ohio, USA) 2400 sourceMeter. Illumination was provided by a Newport Sol3A solar simulator with an AM1.5G spectrum and light intensity of 100 mW/cm^2, which was determined by a calibrated crystalline Si-cell. The external quantum efficiency (EQE) spectra were recorded with by an Enli Technology (Kaohsiung City, Taiwan) EQE measurement system (QE-R), and the light intensity at each wavelength was calibrated with a standard single-crystal Si photovoltaic cell. Patterning of perovskite films for EFM measurements was performed using a commercial laser light scattering device (Wuhan Dr laser technology corp, LTD, Wuhan, China) with a 532 nm laser.

2.5. EFM/SKPM and related measurements

All AFM-based experiments were performed in ambient condition using an MFP-3D-BIO AFM (Asylum Research, Goleta, CA, USA), and Ti/Ir coated silicon tips (ASYELELC-01-R2) with a spring constant of k ~1.4–5.8 N/m, and resonance frequencies of ~58–97 KHz were used in SKPM imaging. Ti/Ir coated silicon tips (AC240TM-R3) with a spring constant of k ~0.3–4.8 N/m and a resonance frequency at ~45–95 KHz were used in conductive atomic force microscopy (C-AFM) imaging. The whole AFM system as integrated with an optical microscope (IX71, Olympus, Shinjuku, Tokyo, Japan), so the sample could be easily illuminated through a 40 × objective in the measurements. The light intensity, as measured by a laser power meter LP1, was approximately 0.01 W cm^{-2} (equivalent to 0.1 suns, but not the AM1.5G spectrum).

EFM measurements were carried out in a two-pass manner. The first pass was used to determine the topography of the surface, and was done in exactly the same way as a standard AC mode scan line in AFM. The second pass was done by retracing the topography at a constant distance of 25 nm in the z direction. The whole AFM system was integrated with an optical microscope (IX71, Olympus, Tokyo, Japan), so the sample could be easily illuminated in the measurements. For EFM, only a constant DC voltage was applied, and the phase shift of the tip was used to measure the electrostatic force between the tip and the sample. As the tip is raised up at a fixed distance from the sample, the major part of the force on the cantilever is due to the long-range tip-sample interactions; e.g., electrostatic force [32,33]. In EFM, the tip and the sample interaction can be treated as a parallel plate capacitor, then the electrostatic force is proportional to the square of the applied voltage. Assuming the voltage between the sample and the probe, and the equivalent capacitance C, the total energy of the system can be interpreted as $U = -1/2C\Delta V^2$.

Conductive AFM is here defined as any current through the sample and the tip of atomic force microscopy. This measures variables in Ohm's equation $V = IZ$, where V is the voltage applied to the sample, I is the current passing through the sample and the tip, and Z is the equivalent resistance of the entire circuit. The setpoint in the contact mode measurements is 0.5 ± 0.02 V.

Different from C-AFM, the scan technique relies on an AC bias applied to the tip to produce an electric force on the cantilever that is proportional to the potential difference between the tip and the sample in SKPM mode.

All the experiments were measured in a similar ambient environment and room temperature.

3. Results and discussion

Fig. 1a shows the device configuration of our planar-inverted PSCs [34]. On the ITO glass substrate, PEDOT:PSS was adopted as a hole transport material while a bilayer of PCBM and ZrAcac was used as the electron transport layer. A 380-nm thick perovskite (intrinsic or doped) film was sandwiched between the two layers (Fig. 1b). Fig. 1c shows a typical contrast between the intrinsic and the Mn^{2+} doped PSC device with the best performance. All devices had negligible hysteresis and a high fill factor, which proves the device quality. In order to figure out the influence of Mn doping in $MAPbI_3$ film on the device performance, a series of Mn dopant concentrations was prepared, which was determined by the Mn/Pb atomic ratio in precursor solution.

Fig. 2a shows the J–V curves of optimal devices with different Mn doping rates ranging from 0% to 2%. PSCs without Mn doping (0%) exhibit an open-circuit voltage (V_{OC}) of 0.890 V, a short-circuit current density (J_{SC}) of 21.13 mA/cm^2, a fill factor (FF) of 67.42%, and a power conversion efficiency (PCE, η) of 12.67%. When the Mn/Pb ratio increases to 0.2%, the device PCE increases significantly to 14.72%, due to the increase in V_{OC} and FF, while J_{SC} is decreased (Voc = 0.91 V, J_{sc} = 20.51 mA/cm^2, FF = 78.63%, and η = 14.72%). As the Mn/Pb ratio rises further to 0.6% and 1%, V_{OC} keep increasing, whereas J_{SC} drops significantly and FF also decreases. When the Mn/Pb ratio reaches 2%, the V_{OC} decreases significantly along with the J_{SC} declining to 7.851 mA/cm^2 and FF decreasing to 35.52%. The hysteresis also becomes significant for 2% doping. With the increase of the doping amount, the short circuit current tends to decrease, while the open circuit voltage first increases and then decreases. The hysteresis effect of the device is very small when there is no doping or low-concentration doping. With the increase of doping concentration, obvious hysteresis will occur. The calculated photocurrent intensities from the spectrum integration in Fig. 2b confirm the deteriorating behavior of the short circuit current density as the doping concentration increases. The integrated values are slightly lower than the corresponding ones in Fig. 2a due to an underestimated spectral mismatch issue [35]. The statistics (average values and standard deviations) of device performances for different Mn concentrations are summarized in Fig. 2c and d.

To explore the mechanisms behind the observed performance changes with increasing doping concentrations, the structure and properties of undoped and doped perovskite films were investigated. Fig. 3a shows the obtained XRD patterns. Regarding the film coated onto the PEDOT:PSS/ITO for all samples, the obtained patterns are consistent with the previous reports for the tetragonal conformation of $MAPbI_3$ (space group I4/mcm, Z = 4), with peaks at 14.03° and 28.40° which are indexed to the (110) and (022) planes, respectively [36,37]. No obvious shift occurred at the main peak at 14.03°, which indicates that the doping concentration within 2% in Mn/Pb does not result in a significant change in the lattice constant. However, the intensity of XRD patterns declines significantly with the increasing Mn/Pb ratio. Furthermore, no Mn was found in the samples by both energy dispersive spectrometry (EDS) and X-ray photoelectronic spectroscopy (XPS) spectra, which indicates that the dopant concentration is below the detection limit of these techniques.

Fig. 3b shows the UV–Vis absorption and photoluminescence (PL) of the samples for different Mn/Pb doping concentrations. A small blue shift of the absorption edge, as well as a small blue shift of the PL peak, is observed with increasing dopant concentration. That is the blue shift in the PL peak emission peak is for the MAPbI3 films with the Mn/Pb ratio ranging from 0% to 2% suggests a higher defect density. From the absorption data and the UPS spectra (Fig. 3c), a schematic diagram of the energy band levels shown in Fig. 3d can be obtained. It can be observed that the valence band (VB) of the perovskite films rises and the bandgap slightly increases with increasing Mn concentration. This results in the reduction of mismatch between the VB of the perovskite and the PEDOT:PSS layer and the enhancement of the hole transport. This in turn results in the enhancement of V_{OC} observed (Fig. 2a,c) [13]. Through TR-PL, the PL lifetime decreases from 491.7 ns for the pristine perovskite to 89.0 ns for the doped film with a 2% Mn/Pb ratio, shown in Fig. 3e and f. Comparing the two different regions of the TRPL process: the initial fast zone (due to trap-assisted non-radiative decay) and the slow zone (due to radiative recombination of free charge carriers). It can be found that the trap density of Mn doped perovskite films is higher. compared with the original perovskite film. The reduced carrier lifetime indicates increased recombination, which results in a J_{SC} decrease. The likely cause of reduced lifetime is reduced crystallinity (in agreement with the observed reduction in the intensity of XRD

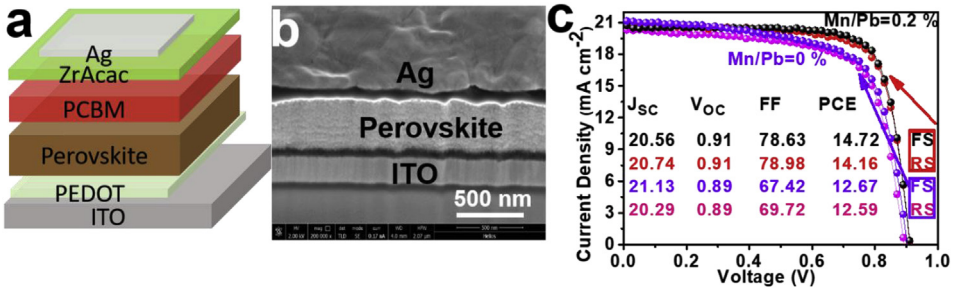

Fig. 1. (**a**) Device configuration and (**b**) cross-section scanning electron microscopy (SEM) image of planar PSCs in this work. (**c**) Typical J–V curves of devices based on intrinsic and doped perovskite materials. In the doped perovskite film, the Mn/Pb molar ratio in precursor solution is 0.2% (reverse scan (RS) and forward scan (FS)).

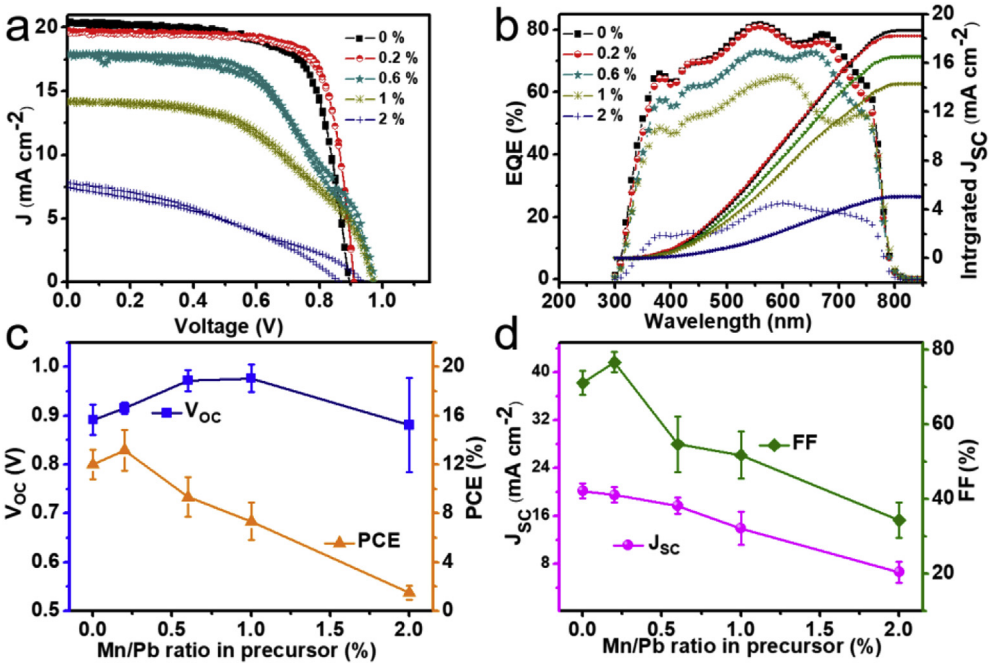

Fig. 2. The device performance for perovskite layers with Mn/Pb ratios of 0%, 0.2%, 0.6%, 1% and 2%. (**a**) J − V curves, (**b**) EQE spectra under 1 sun illumination (100 mW/cm^2). (**c**,**d**) Statistical performance parameters of PSCs with different Mn concentrations summarized from a batch of 36 devices for each kind.

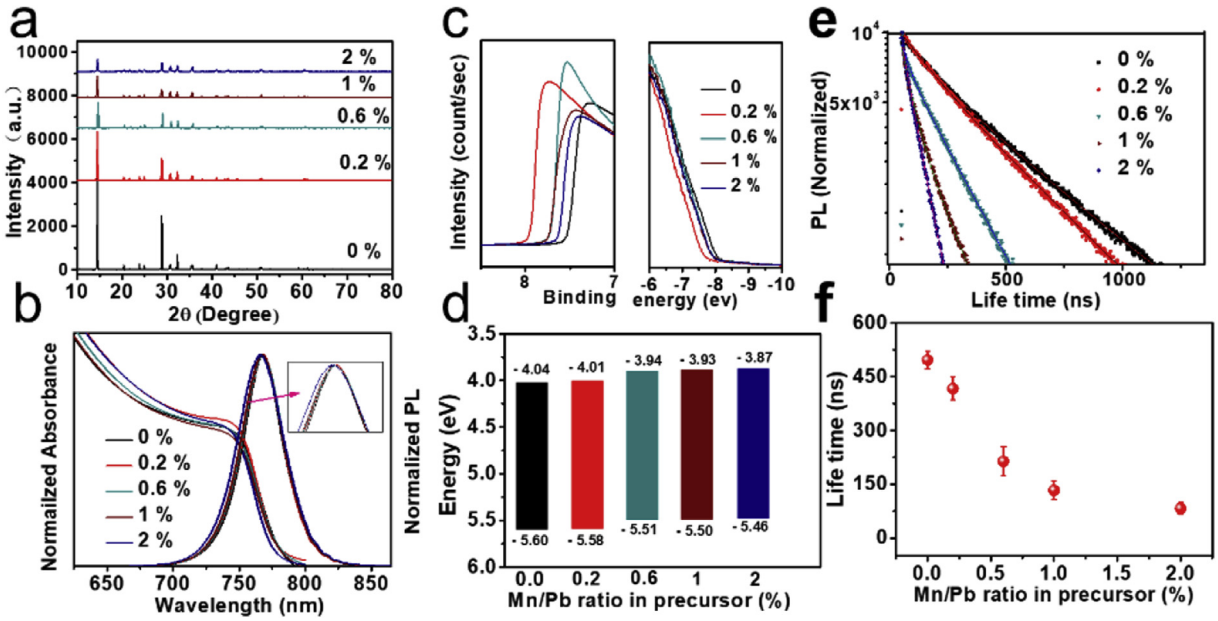

Fig. 3. (**a–f**) The characterization of $MAPbI_3$ films with the Mn/Pb ratio ranging from 0% to 2% (**a**) X-ray diffraction (XRD) patterns; (**b**) UV–visible absorption and normalized PL spectra with magnified PL peaks as inset; (**c**) ultraviolet photoelectron spectroscopy (UPS) spectra; and (**d**) energy band diagram; (**e**) time-resolved photoluminescence (TR-PL) spectra of the five kinds of perovskite films coated on glass substrate under excitation by a 405 nm laser; (**f**) statistics of the fluorescence lifetime of those films.

patterns), which results in increased grain boundaries and defects, and consequently reduced mobility and increased non-radiative recombination centers [38–44]. In comparison to the pristine sample, the doping of 0.2% films featured small grains with a long lifetime. There are similarities between this and what has been reported in the relevant literature [45]. In addition, the grain boundaries may also affect the charge recombination [46].

Although the variations of V_{OC} and J_{SC} with the increasing doping concentration are well explained by the above characterizations, the effect on the fill factor of devices is still not fully clear. Therefore, the surface morphology evolution in the series of perovskite films was also investigated (Fig. 4). Fig. 4a shows a typical surface morphology of $MAPbI_3$ film spin-coated on the surface of PEDOT/ITO substrates. For 0.2% doping, the grain size reduced and the grain boundaries multiplied while the overall morphology (grain shape) did not exhibit a significant change (Fig. 4b). However, with a further increase in the doping concentration to 0.6%, the surface roughness increased and pinholes could be observed (Fig. 4c). When the doping concentration increased further, the crystallinity degraded and the elongated grain shape becomes more pronounced; additionally, the grain crystallinity degrades sharply (Fig. 4d and e). The similar changes in morphology were reported recently for the increasing alloying concentration

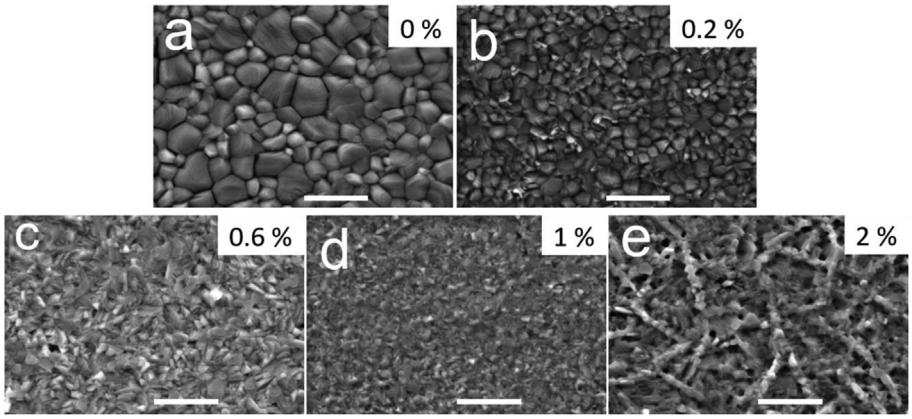

Fig. 4. Typical SEM image of the surface morphology of perovskite films coated on the surface of PEDOT:PSS/ITO substrates for Mn/Pb ratios of 0% (**a**), 0.2% (**b**), 0.6% (**c**), 1% (**d**), 2% (**e**). The scale bar is 1 μm.

(5–25%) of manganese in $MAPbI_3$ film [47]. Simultaneously, to exclude the possibility that the major contribution of the structure evolution is from chloride ions, a reference film with $PbCl_2$ instead of $MnCl_2$ was prepared. Its surface image shows no elongated grain morphology, except for an emerging of PbI_2 nanocrystals (Figure S1).

In our work, the intrinsic film (Fig. 5a) with the largest perovskite grain size shows the lowest V_{OC}, while the 0.2%—Mn doped film (Fig. 5d) with the smallest grain size shows the highest V_{OC}. It was previously reported that the V_{OC} could increase with decreased grain size [25]. To investigate this phenomenon, we applied SKPM (in the dark and under illumination), C-AFM, and EFM techniques to follow the evolution of the surface potential, surface current and surface charge of the perovskite films with different Mn/Pb ratios (0%, 0.2%). The obtained SKPM images are shown in Fig. 5. The perovskite surface is directly accessible by the scanning probe while the ITO layer is grounded. Open-circuit conditions are applied similar to those used in a previous report [25,48]. SKPM measurement confirmed the presence of a photovoltaic effect for the perovskite film, and the average potential differences (ΔV) between the dark and illuminated condition are related to the photoresponse of the perovskite film. The surface potentials of intrinsic and Mn-doped (0.2%) perovskite films are −124.6 mV (Fig. 5b) and −79.1 mV (Fig. 5e) in the dark, respectively. Under light illumination, the surface potentials are −231.8 mV (Fig. 5c) and −212.2 mV (Fig. 5f), respectively. This difference indicates that the work function of the perovskite film increases upon the light illumination [49]. In addition, it indicates that the work function of perovskite films is increased after doping with Mn. The increasing work function demonstrates that electrons from perovskite film could be extracted more easily [50]. The average differences in surface potential (ΔV) between the samples under illumination and in the dark were calculated. The results show ΔV of 107.2 and 133.1 mV for intrinsic and Mn-doped (0.2%) samples, respectively. The higher surface potential difference of the Mn doped perovskite film could be a factor enhancing the V_{OC}. To further characterize intrinsic and 0.2% Mn-doped samples, C-AFM measurements were performed in the dark to determine the electronic properties of those perovskite films. Figure S2a,b shows the current mapping of the two samples, which clearly shows that when the doping concentration increases, the bulk conductivity decreases. Although the resolution is not high enough to distinguish the grain-dependent resolution of conductivity mapping of doped perovskite films, the average bulk conductivity indicates the trend of doping effect, declining from 67.4 ± 2.5 pA to 65.1 ± 1.5 pA. This is different from expectation that doping would increase the concentration of the majority carriers and hence enhance the conductivity [51–53]. This is due

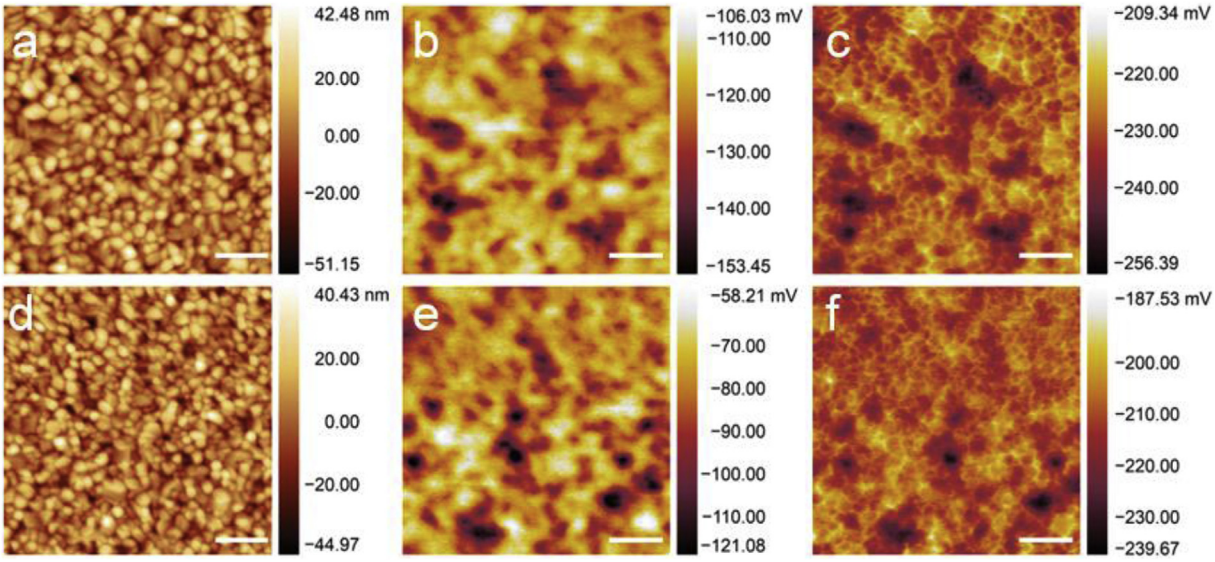

Fig. 5. Topographic morphology image (**a**), dark-scanning Kelvin probe microscopy (SKPM) image (**b**) and light-SKPM image (**c**) of Mn/Pb ratio of 0%/PEDOT/ITO glass; Topographic morphology image (**d**), dark-SKPM image (**e**) and light-SKPM image (**f**) of Mn/Pb ratio of 0.2%/PEDOT/ITO glass. The scanning scales are 5 μm × 5 μm and the scale bar is 1 μm.

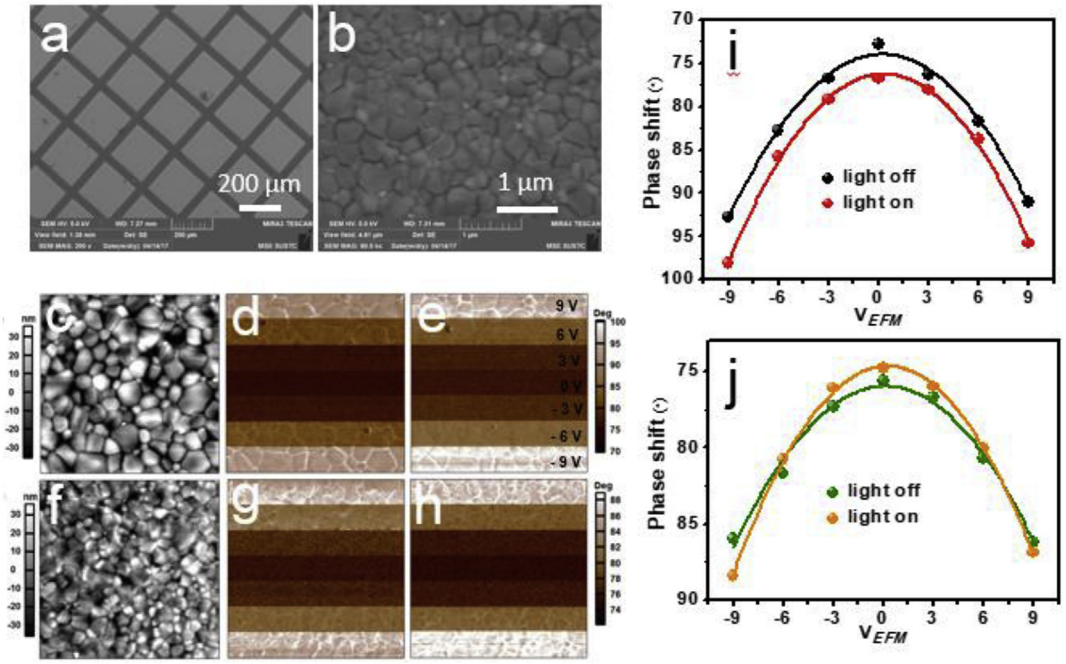

Fig. 6. Low (**a**) and high (**b**) magnification SEM images of the 0.2% Mn/Pb-doped perovskite film spin-coated on bare glass substrates after laser scribing; (**c**) atomic force microscopy (AFM) image of pristine perovskite film; (**d**,**e**) electrostatic force microscopy (EFM) images of pristine perovskite film (**d**) dark and (**e**) light under a bias voltage of 9 V, 6 V, 3 V, 0 V and −3 V, −6 V, −9 V; (**f**) AFM images of the 0.2% Mn/Pb doped perovskite film; (**g**,**h**) EFM images of the 0.2% Mn/Pb doped perovskite film under (**g**) dark and (**h**) light conditions under a bias voltage of −3 V, 0 V and 3 V, respectively. The scale bar is 1 μm; (**i**) pristine perovskite film and (**j**) 0.2% Mn/Pb doped perovskite film phase shift Δø vs. EFM bias V_{EFM} with the light off and light on. The curves are the best fit for the polynomial law of Equation (1).

to the fact that conductivity is proportional to both carrier concentration and mobility, and the worsening of the crystallinity (Figs. 3a and 4) would result in decreased mobility. In addition, the effects of the dopant on the carrier concentration are not fully clear due to having the same valence of Mn^{2+} and Pb^{2+}, combined with the complex processes of charge transport in perovskites, including the low activation energy of defects and mobile ions of MA and idodine [54–58]; it is therefore not easy to determine whether electrons or holes are the majority carriers [3,10,59–61].

Therefore, EFM was used to reveal directly the relationship between doping and carrier concentration in our perovskite films. According to the sample configuration requirement in EFM tests, semiconductor materials must be isolated islands on/in the insulator substrate, which can simplify the source of induced charges [26,28–30]. To prepare the samples for EFM test, a 532 nm laser was used to scribe the perovskite film into patterned separated islands (Fig. 6a). Fig. 6b shows the typical surface morphology of the 0.2% Mn/Pb-doped perovskite film deposited directly on bare glass, where the grain size is larger than that on PEDOT/ITO substrates. The good quality of the two kinds of films tested simplifies the analysis of that relationship, excluding the influence of various defects and sources.

Fig. 6d and e shows the mapping of the phase shift of the pristine perovskite film at bias voltages of 9 V, 6 V, 3 V, 0 V, −3 V, −6 V, and −9 V with the light off and on, respectively. When ± 9 V, ± 6 V, and ± 3 V bias voltages are applied, the phase shift mapping has a contrast with that of no bias voltage, and V_{EFM} is brighter at negative bias voltages. For the 0.2% Mn/Pb-doped perovskite film (Fig. 6g and h), the phase shift of +9 V in V_{EFM} is lower than that of −9 V when the light is off, while the opposite occurs when the light is on. Moreover, the phase shift of the doped perovskite film is obviously smaller than that of the pristine one under the high bias voltage. With the relationship between the phase shift $\Delta\phi$ and the bias voltage (V_{EFM}), the function in an approximate capacity model can be fitted by Equation (1) as follows [62], where $\Delta\phi$ is the phase shift of the resonant peak (degree):

$$\Delta\phi = K_0 + K_1 V_{EFM} + K_2 V_{EFM}^2 \quad (1)$$

The constants K_1 and K_2 can be defined as follows [28,31]:

$$K_1 = \frac{Q}{2k}\left[\frac{qh}{(\varepsilon z^3)}\right]; \quad K_2 = -\frac{Q}{2k}\left[\frac{3\varepsilon_0 Sh}{z^4}\right]; \quad (2)$$

where Q is the quality factor, k is the spring constant of the cantilever, z is the tip–surface distance, q is the surface charge, ε is dielectric constant, and ε_0 vacuum dielectric constant. K_1 is proportional to q, the quantity of charge induced by V_{EFM} [31].

Based on the above model, the relationship between the phase shift and V_{EFM} of the pristine and doped perovskite films is fitted and shown in Fig. 6i and j. For the pristine perovskite film in the dark, $K_1 = -0.09°/V$ and $K_2 = 0.22°/V^2$. When the light is turned off, $K_1 = -0.14°/V$ and $K_2 = 0.25°/V^2$ are obtained. For the 0.2% Mn/Pb-doped perovskite film, the values of $K_1 = -0.07°/V$, $K_2 = 0.16\ °/V^2$ and $K_1 = -0.02°/V$, $K_2 = 0.03°/V^2$ are obtained when the light is on and off, respectively (Table 1). Because the same cantilever and tip are used for both samples, the surface charges obtained are also proportional to the surface charge density of the sample. From the obtained data, we can conclude that surface charge density is positive in the perovskite film in the dark, and it is also positive with the light on. In addition, the surface charge density increases under illumination, as

Table 1
Fitting results obtained by fitting ΔΦ—V_{EFM} curves of perovskite film with Equation (1).

	K_1	K_2	K_1/K_2
0% off	−0.09	0.22	0.49
0% on	−0.14	0.25	0.56
0.2% off	−0.02	0.16	0.67
0.2% on	−0.07	0.03	0.43

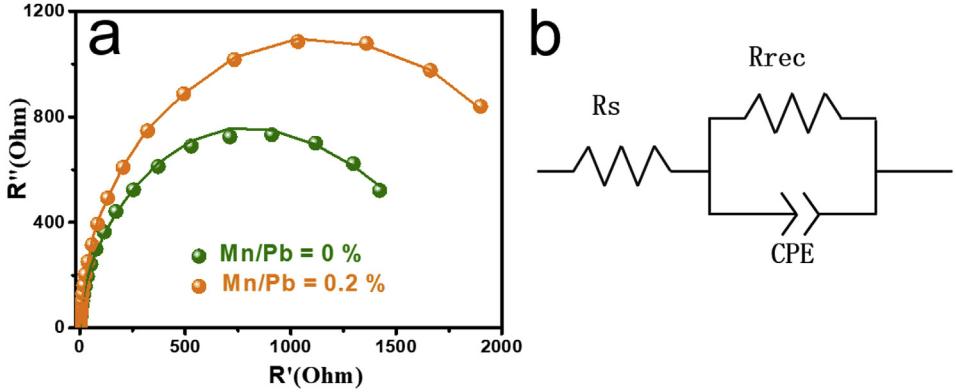

Fig. 7. (**a**) Nyquist plots obtained from the electrochemical impedance spectroscopy (EIS) measurement of perovskite solar cells with Mn/Pb ratio of 0%, 0.2% without illumination; (**b**) equivalent circuit employed to fit the EIS data.

expected due to the photogeneration of charge carriers. Finally, whether the light is off or on, the surface charge density of the pristine films is larger than that of the doped perovskite films, in agreement with the measured short circuit current density.

For a deeper insight into the influence of doped/undoped PSC performance, electrochemical impedance spectroscopy (EIS) measurements were carried out to be investigated. Fig. 7 shows the Nyquist plots obtained for the systematically analyzed cells [61]. The results correspond to the doped and undoped solar cells, both under dark conditions. The impedance spectra are dominated by a large semicircle. From the impedance spectra, we can extract the series resistance (Rs) and the charge recombination resistance (Rrec) in the devices. After the fitting of the EIS data with equivalent circuit shown in Fig. 7, Rs of 2.12 Ω and Rrec of 1542 Ω can be obtained for undoped devices. The slightly reduced Rs of 1.83 Ω and increased Rrec of 2312 Ω for Mn^{2+} doped devices indicate the small dose of doping of Mn^{2+} is able to reduce the series resistance and suppress the charge recombination. As a result, the device performances can be improved after Mn^{2+} doping, which is well consistent with our experimental results. At last, the stability of assembled perovskite solar cells for Mn/Pb ratios of 0% and 0.2% are displayed in Figure S3. The obtained results show that the degradation rate of the Mn^{2+}-doped PSC device is relatively larger than the undoped PSC after 24 h of illumination. That is, the stability of perovskite solar cells will be reduced by the introduction of Mn^{2+} in continuous illumination. The deterioration of the device lifetime by Mn doping in perovskite could be attributed to at least two factors. One is that more grain boundaries were yielded from the doping, which is shown in Fig. 4. More grain boundaries lead to the higher possibility of infiltration of hydromolecules and the degradation of perovskite materials. The other is that doping derived defects in either the interior or the grain boundaries of perovskite grains, which might accelerate the device degradation.

4. Conclusions

In summary, we have systematically investigated the Mn^{2+} doping effect of $MAPbI_3$ perovskite on the film morphology, device performance as well as the photoelectronic properties with various techniques. We have demonstrated that the device performance could be improved for a low Mn^{2+} dopant concentration in $MAPbI_3$ perovskite via enhancing the V_{OC} and FF, while the J_{SC} always continued to decrease. Multi-functional AFM techniques, such as SKPM, EFM and C-AFM, were used to correlate the photo-generated current and surface potential variation before and after manganese doping in the perovskite film. This paper demonstrates the usefulness of scanning probe techniques for investigating the doping effect in organic–inorganic perovskite films.

Author contributions

Conceptualization, Data analysis, Writing—original draft, Y.W.; Data analysis, W.C., Z.W. and X.F.; Supervision, L.L. and G.C.; Writing—review and editing, A.B-D, R.L. and Z.H.

Conflicts of interest

The authors declare no conflicts of interest.

Appendix A. Supplementary data

Supplementary data to this article can be found online at https://doi.org/10.1016/j.jpowsour.2019.04.009.

Funding

This work was supported by the National Natural Science Foundation of China (Grant No. No. 11674043, No. 11604030, No. 61775091), The Fundamental Research Funds for the Central universities (2018CDJDWL0011), the National Key Research Project MOST (No. 2016YFA0202400), Natural Science Foundation of Shenzhen Innovation Committee (No. JCYJ20150529152146471), and the Shenzhen Key Laboratory Project (No. ZDSYS201602261933302).

References

[1] NREL, Available online: http://www.nrel.gov/pv/assets/images/efficiency_chart.jpg , Accessed date: 1 March 2019.
[2] H. Zhang, H. Wang, S.T. Williams, D. Xiong, W. Zhang, C.C. Chueh, W. Chen, A.K. Jen, $SrCl_2$ derived perovskite facilitating a high efficiency of 16% in hole-conductor-free fully printable mesoscopic perovskite solar cells, Adv. Mater. 29 (2017) 1606608.
[3] M. Jahandar, J.H. Heo, C.E. Song, K.-J. Kong, W.S. Shin, J.-C. Lee, S.H. Im, S.-J. Moon, Highly efficient metal halide substituted CH3NH3I(PbI2)1 − X(CuBr2) X planar perovskite solar cells, Nanomater. Energy 27 (2016) 330–339.
[4] Y. Hu, E.M. Hutter, P. Rieder, I. Grill, J. Hanisch, M.F. Aygüler, A.G. Hufnagel, M. Handloser, T. Bein, A. Hartschuh, et al., Understanding the role of cesium and rubidium additives in perovskite solar cells: trap states, charge transport, and recombination, Adv. Energy Mater. (2018) 1703057, https://doi.org/10.1002/aenm.201703057.
[5] M. Abdi-Jalebi, Z. Andaji-Garmaroudi, S. Cacovich, C. Stavrakas, B. Philippe, J.M. Richter, M. Alsari, E.P. Booker, E.M. Hutter, A.J. Pearson, et al., Maximizing and stabilizing luminescence from halide perovskites with potassium passivation, Nature 555 (2018) 497–501.
[6] D. Chen, G. Fang, X. Chen, L. Lei, J. Zhong, Q. Mao, S. Zhou, J. Li, Mn-Doped $CsPbCl_3$ perovskite nanocrystals: solvothermal synthesis, dual-color luminescence and improved stability, J. Mater. Chem. C 6 (2018) 8990–8998.
[7] G. Volonakis, M.R. Filip, A.A. Haghighirad, N. Sakai, B. Wenger, H.J. Snaith, F. Giustino, Lead-free halide double perovskites via heterovalent substitution of noble metals, J. Phys. Chem. Lett. 7 (2016) 1254–1259.
[8] Y. Bai, Y. Fang, Y. Deng, Q. Wang, J. Zhao, X. Zheng, Y. Zhang, J. Huang, Low temperature solution-processed $Sb:SnO_2$ nanocrystals for efficient planar perovskite solar cells, ChemSusChem (2016), https://doi.org/10.1002/cssc.201600944.

[9] J.T.-W. Wang, Z. Wang, S. Pathak, W. Zhang, D.W. deQuilettes, F. Wisnivesky-Rocca-Rivarola, J. Huang, P.K. Nayak, J.B. Patel, H.A. Mohd Yusof, et al., Efficient perovskite solar cells by metal ion doping, Energy Environ. Sci. 9 (2016) 2892–2901.

[10] M. Abdi-Jalebi, M.I. Dar, A. Sadhanala, S.P. Senanayak, M. Franckevičius, N. Arora, Y. Hu, M.K. Nazeeruddin, S.M. Zakeeruddin, M. Grätzel, et al., Impact of monovalent cation halide additives on the structural and optoelectronic properties of CH3NH3PbI3Perovskite, Adv. Energy Mater. 6 (2016) 1502472.

[11] K.M. Boopathi, R. Mohan, T.-Y. Huang, W. Budiawan, M.-Y. Lin, C.-H. Lee, K.-C. Ho, C.-W. Chu, Synergistic improvements in stability and performance of lead iodide perovskite solar cells incorporating salt additives, J. Mater. Chem. A 4 (2016) 1591–1597.

[12] Y. Zhou, Z. Zhou, M. Chen, Y. Zong, J. Huang, S. Pang, N.P. Padture, Doping and alloying for improved perovskite solar cells, J. Mater. Chem. A 4 (2016) 17623–17635.

[13] W. Zhao, Z. Yao, F. Yu, D. Yang, S. Liu, Alkali metal doping for improved $CH_3NH_3PbI_3$ perovskite solar cells, Adv. Sci. 5 (2018) 1700131.

[14] D.-Y. Son, S.-G. Kim, J.-Y. Seo, S.-H. Lee, H. Shin, D. Lee, N.-G. Park, Universal approach toward hysteresis-free perovskite solar cell via defect engineering, J. Am. Chem. Soc. 140 (2018) 1358–1364.

[15] M.T. Klug, A. Osherov, A.A. Haghighirad, S.D. Stranks, P.R. Brown, S. Bai, J.T.W. Wang, X. Dang, V. Bulović, H.J. Snaith, et al., Tailoring metal halide perovskites through metal substitution: influence on photovoltaic and material properties, Energy Environ. Sci. 10 (2017) 236–246.

[16] L.A. Frolova, D.V. Anokhin, K.L. Gerasimov, N.N. Dremova, P.A. Troshin, Exploring the effects of the Pb^{2+} substitution in $MAPbI_3$ on the photovoltaic performance of the hybrid perovskite solar cells, J. Phys. Chem. Lett. 7 (2016) 4353–4357.

[17] E.J. Spadafora, R. Demadrille, B. Ratier, B. Grévin, Imaging the carrier photogeneration in nanoscale phase segregated organic heterojunctions by Kelvin probe force microscopy, Nano Lett. 10 (2010) 3337–3342.

[18] M. Nonnenmacher, M.P. Oboyle, H.K. Wickramasinghe, Kelvin probe force microscopy, Appl. Phys. Lett. 58 (1991) 2921–2923.

[19] J. Cao, B. Wu, R. Chen, Y. Wu, Y. Hui, B.W. Mao, N. Zheng, Efficient, hysteresis-free, and stable perovskite solar cells with ZnO as electron-transport layer: effect of surface passivation, Adv. Mater. 30 (2018) 1705596.

[20] P.F. Siles, M. Devarajulu, F. Zhu, O.G. Schmidt, Direct imaging of space-charge accumulation and work function characteristics of functional organic interfaces, Small 14 (2018) 1703647.

[21] G. Xu, R. Xue, W. Chen, J. Zhang, M. Zhang, H. Chen, C. Cui, H. Li, Y. Li, Y. Li, New strategy for two-step sequential deposition: incorporation of hydrophilic fullerene in second precursor for high-performance p-i-n planar perovskite solar cells, Adv. Energy Mater. (2018) 1703054, https://doi.org/10.1002/aenm.201703054.

[22] C.E. Smith, Z. Xie, I. Baldea, C.D. Frisbie, Work function and temperature dependence of electron tunneling through an N-type perylene diimide molecular junction with isocyanide surface linkers, Nanoscale 10 (2018) 964–975.

[23] J. Hieulle, C. Stecker, R. Ohmann, L.K. Ono, Y. Qi, Scanning probe microscopy applied to organic–inorganic halide perovskite materials and solar cells, Small Met 2 (2018) 1700295.

[24] Y. Wu, P. Wang, S. Wang, Z. Wang, B. Cai, X. Zheng, Y. Chen, N. Yuan, J. Ding, W.H. Zhang, Heterojunction engineering for high efficiency cesium formamidinium double-cation lead halide perovskite solar cells, ChemSusChem 11 (2018) 837–842.

[25] Z. Zhao, X. Chen, H. Wu, X. Wu, G. Cao, Probing the photovoltage and photocurrent in perovskite solar cells with nanoscale resolution, Adv. Funct. Mater. 26 (2016) 3048–3058.

[26] T. Mélin, H. Diesinger, D. Deresmes, D. Stiévenard, Electric force microscopy of individually charged nanoparticles on conductors: an analytical model for quantitative charge imaging, Phys. Rev. B 69 (2004) 035321.

[27] K.A.S. Araujo, L.A. Cury, M.J.S. Matos, T.F.D. Fernandes, L.G. Cancado, B.R.A. Neves, Electro-optical interfacial effects on a graphene/pi-conjugated organic semiconductor hybrid system, Beilstin J. Nanotechnol. 9 (2018) 963–974.

[28] H. Xuan, X. Chen, Y. Wu, K. Song, Y. Li, R. Liu, Charges on nano-islands and fibrils of poly(3-hexylthiophene-2,5-diyl)-light-modulation, injection and transportation, RSC Adv. 6 (2016) 15577–15584.

[29] T. Heim, K. Lmimouni, D. Vuillaume, Ambipolar charge injection and transport in a single pentacene monolayer island, Nano Lett. 4 (2004) 2145–2150.

[30] S.E. Yalcin, J.A. Labastide, D.L. Sowle, M.D. Barnes, Spectral properties of multiply charged semiconductor quantum dots, Nano Lett. 11 (2011) 4425–4430.

[31] S. Wu, Z. Wu, D. Lin, Z. Zhong, Z. Jiang, X. Yang, Photogenerated charges and surface potential variations investigated on single Si nanorods by electrostatic force microscopy combined with laser irradiation, Nanoscale Res. Lett. 9 (2014) 245.

[32] J. Kim, W.J. Jasper, J.P. Hinestroza, Charge characterization of an electrically charged fiber via electrostatic force microscopy, J. Eng. Fibers Fabr. 1 (2006) 30–46.

[33] J. Kim, W. Jasper, R.L. Barker, J.P. Hinestroza, Application of electrostatic force microscopy on characterizing an electrically charged fiber, Fibers Polym. 11 (2010) 775–781.

[34] W. Chen, L. Xu, X. Feng, J. Jie, Z. He, Metal acetylacetonate series in interface engineering for full low-temperature-processed, high-performance, and stable planar perovskite solar cells with conversion efficiency over 16% on 1 cm^2 scale, Adv. Mater. 29 (2017) 1603923.

[35] W. Chen, Y. Zhu, Y. Yu, L. Xu, G. Zhang, Z. He, Low cost and solution processed interfacial layer based on poly(2-ethyl-2-oxazoline) nanodots for inverted perovskite solar cells, Chem. Mater. 28 (2016) 4879–4883.

[36] X. Feng, H. Su, Y. Wu, H. Wu, J. Xie, X. Liu, J. Fan, J.-F. Dai, Z. He, Photon-generated carriers excited superoxide species inducing long-term photoluminescence enhancement of $MAPbI_3$ perovskite single crystals, J. Mater. Chem. A 5 (2017) 12048–12053.

[37] L. Xi, C.B. Boothroyd, T. Salim, S. Borghardt, Y.M. Lam, B.E. Kardynal, Facile in situ synthesis of stable luminescent organic-inorganic lead halide perovskite nanoparticles in a polymer matrix, J. Mater. Chem. C 5 (2017) 7207–7214.

[38] M. Yang, Y. Zeng, Z. Li, D.H. Kim, C.S. Jiang, J. van de Lagemaat, K. Zhu, Do grain boundaries dominate non-radiative recombination in CH3NH3PbI3 perovskite thin films? Phys. Chem. Chem. Phys. 19 (2017) 5043–5050.

[39] S. Zhang, S. Wu, W. Chen, H. Zhu, Z. Xiong, Z. Yang, C. Chen, R. Chen, L. Han, W. Chen, Solvent engineering for efficient inverted perovskite solar cells based on inorganic $CsPbI_2Br$ light absorber, Mater. Today Energy 8 (2018) 125–133.

[40] V.C. Nair, C. Muthu, A.L. Rogach, R. Kohara, V. Biju, Channeling exciton migration into electron transfer in formamidinium lead bromide perovskite nanocrystal/fullerene composites, Angew. Chem. Int. Ed. 56 (2017) 1214–1218.

[41] N.K. Noel, A. Abate, S.D. Stranks, E.S. Parrott, V.M. Burlakov, A. Goriely, H.J. Snaith, Enhanced photoluminescence and solar cell performance via lewis base passivation of organic inorganic lead halide perovskites, ACS Nano 8 (2014) 9815–9821.

[42] F. Deschler, M. Price, S. Pathak, L.E. Klintberg, D.D. Jarausch, R. Higler, S. Huttner, T. Leijtens, S.D. Stranks, H.J. Snaith, et al., High photoluminescence efficiency and optically pumped lasing in solution-processed mixed halide perovskite semiconductors, J. Phys. Chem. Lett. 5 (2014) 1421–1426.

[43] S.D. Stranks, V.M. Burlakov, T. Leijtens, J.M. Ball, A. Goriely, H.J. Snaith, Recombination kinetics in organic-inorganic perovskites: excitons, free charge, and subgap states, Phys. Rev. Appl. 2 (2014) 034007.

[44] C.M. Wolff, F. Zu, A. Paulke, L.P. Toro, N. Koch, D. Neher, Reduced interface-mediated recombination for high open-circuit voltages in $CH_3NH_3PbI_3$ solar cells, Adv. Mater. (2017), https://doi.org/10.1002/adma.201700159.

[45] A. Fakharuddin, M. Seybold, A. Agresti, S. Pescetelli, F. Matteocci, M.I. Haider, S.T. Birkhold, H. Hu, R. Giridharagopal, M. Sultan, et al., Perovskite-Polymer blends influencing microstructures, nonradiative recombination pathways, and photovoltaic performance of perovskite solar cells, ACS Appl. Mater. Interfaces 10 (2018) 42542–42551.

[46] R. Ciesielski, F. Schäfer, N.F. Hartmann, N. Giesbrecht, T. Bein, P. Docampo, A. Hartschuh, Grain boundaries act as solid walls for charge carrier diffusion in large crystal MAPI thin films, ACS Appl. Mater. Interfaces 10 (2018) 7974–7981.

[47] S.T. Williams, A. Rajagopal, S.B. Jo, C.C. Chueh, T.F.L. Tang, A. Kraeger, A.K.Y. Jen, Realizing a new class of hybrid organic-inorganic multifunctional perovskite, J. Mater. Chem. A 5 (2017) 10640–10650.

[48] J.S. Yun, A. Ho-Baillie, S. Huang, S.H. Woo, Y. Heo, J. Seidel, F. Huang, Y.-B. Cheng, M.A. Green, Benefit of grain boundaries in organic-inorganic halide planar perovskite solar cells, J. Phys. Chem. Lett. 6 (2015) 875–880.

[49] J. Chang, H. Zhu, J. Xiao, F.H. Isikgor, Z. Lin, Y. Hao, K. Zeng, Q.-H. Xu, J. Ouyang, Enhancing the planar heterojunction perovskite solar cell performance through tuning the precursor ratio, J. Mater. Chem. A 4 (2016) 7943–7949.

[50] W. Chen, Y. Zhou, L. Wang, Y. Wu, B. Tu, B. Yu, F. Liu, H.-W. Tam, G. Wang, A.B. Djurišić, et al., Molecule-doped nickel oxide: verified charge transfer and planar inverted mixed cation perovskite solar cell, Adv. Mater. 30 (2018) 1800515.

[51] W. Chen, K. Li, Y. Wang, X. Feng, Z. Liao, Q. Su, X. Lin, Z. He, Black phosphorus quantum dots for hole extraction of typical planar hybrid perovskite solar cells, J. Phys. Chem. Lett. 8 (2017) 591–598.

[52] J.H. Kim, P.W. Liang, S.T. Williams, N. Cho, C.C. Chueh, M.S. Glaz, D.S. Ginger, A.K. Jen, High-performance and environmentally stable planar heterojunction perovskite solar cells based on a solution-processed copper-doped nickel oxide hole-transporting layer, Adv. Mater. 27 (2015) 695–701.

[53] Y. Kutes, Y.Y. Zhou, J.L. Bosse, J. Steffes, N.P. Padture, B.D. Huey, Mapping the photoresponse of CH3NH3PbI3 hybrid perovskite thin films at the nanoscale, Nano Lett. 16 (2016) 3434–3441.

[54] Y. Yuan, Q. Wang, Y. Shao, H. Lu, T. Li, A. Gruverman, J. Huang, Electric-field-driven reversible conversion between methylammonium lead triiodide perovskites and lead iodide at elevated temperatures, Adv. Energy. Mater. 6 (2016) 1501803.

[55] Z. Xiao, Y. Yuan, Y. Shao, Q. Wang, Q. Dong, C. Bi, P. Sharma, A. Gruverman, J. Huang, Giant switchable photovoltaic effect in organometal trihalide perovskite devices, Nat. Mater. 14 (2015) 193–198.

[56] M. De Bastiani, G. Dell'Erba, M. Gandini, V. D'Innocenzo, S. Neutzner, A.R.S. Kandada, G. Grancini, M. Binda, M. Prato, J.M. Ball, Ion migration and the role of preconditioning cycles in the stabilization of the J–V characteristics of inverted hybrid perovskite solar cells, Adv. Energy Mater. 6 (2016) 1501453.

[57] T. Leijtens, E.T. Hoke, G. Grancini, D.J. Slotcavage, G.E. Eperon, J.M. Ball, M. De Bastiani, A.R. Bowring, N. Martino, K. Wojciechowski, Mapping electric field-induced switchable poling and structural degradation in hybrid lead halide perovskite thin films, Adv. Energy Mater. 5 (2015) 1500962.

[58] Y. Yuan, J. Chae, Y. Shao, Q. Wang, Z. Xiao, A. Centrone, J. Huang, Photovoltaic switching mechanism in lateral structure hybrid perovskite solar cells, Adv. Energy Mater. 5 (2015) 1500615.

[59] W. Liu, Q. Lin, H. Li, K. Wu, I. Robel, J.M. Pietryga, V.I. Klimov, Mn^{2+}-Doped lead halide perovskite nanocrystals with dual-color emission controlled by halide content, J. Am. Chem. Soc. 138 (2016) 14954–14961.

[60] T. Singh, A. Kulkarni, M. Ikegami, T. Miyasaka, Effect of electron transporting layer on bismuth-based lead-free perovskite $(CH_3NH_3)_3\ Bi_2I_9$ for photovoltaic applications, ACS Appl. Mater. Interfaces 8 (2016) 14542–14547.

[61] Q. Wu, P. Zhou, W. Zhou, X. Wei, T. Chen, S. Yang, Acetate salts as nonhalogen additives to improve perovskite film morphology for high-efficiency solar cells, ACS Appl. Mater. Interfaces 8 (2016) 15333–15340.

[62] G. Wang, Y. Xi, H. Xuan, R. Liu, X. Chen, L. Cheng, Hybrid nanogenerators based on triboelectrification of a dielectric composite made of lead-free $ZnSnO_3$ nanocubes, Nanomater. Energy 18 (2015) 28–36.